Article

Temperature-Dependent Hydrogenation, Hydrodeoxygenation, and Hydrogenolysis of Anisole on Nickel Catalysts

Shuya Zhang [1,†], Xiaochen Liu [1,2,†], Yuanjie Xu [1,*] and Yu Tang [1,*]

1 Institute of Molecule Catalysis and In-Situ/Operando Studies, College of Chemistry, Fuzhou University, Fuzhou 350108, China
2 Zhejiang Research Institute of Chemical Industry, Hangzhou 310023, China
* Correspondence: n191310059@fzu.edu.cn (Y.X.); yu.tang@fzu.edu.cn (Y.T.)
† These authors contributed equally to this work.

Abstract: Hydrogenation stands out as one of the most promising techniques for converting biomass-derived molecules into valuable products. The expected products of upgrading biomass molecules include hydrocarbon, oxygenate, and methane. Ni-based catalysts have attracted considerable interest owing to their unique properties and relatively low cost. In this work, NiO prepared by the calcination and urea precipitation methods, namely NiO–C and NiO–U, is investigated for the hydrogenation of anisole. It is found that reaction temperature exerts a significant influence on the hydrogenation pathways. At 150 °C, C–reduced NiO proves more inclined towards hydrogenation, while U–reduced NiO demonstrates a tendency for hydrodeoxygenation (HDO). Moreover, as the temperature rises, both nickel catalysts change the reaction route to hydrogenolysis and eventually only produce methane at 300 °C, whereas metallic Ni is formed as the catalytic active phase. In situ FTIR experiments suggest the hydrogenolysis pathway and the formation of methane. This work investigates a route to produce methane from biomass molecules.

Keywords: nickel-based catalysts; hydrodeoxygenation; hydrogenation; hydrogenolysis; methane

1. Introduction

Searching for alternative renewable energy sources has become essential due to the recent depletion in the oil supply available worldwide [1–3]. Biomass is potentially the world's largest sustainable energy source, with 220 billion dry tons available annually. It is currently the only sustainable source of organic carbon and biofuels [4,5]. Thermochemical processes such as pyrolysis can convert biomass directly into bio-oil. However, its low calorific value, thermal instability, and the presence of sulfur, nitrogen, and oxygen heteroatoms hinder its application [6–10]. Therefore, an upgrading process is necessary to increase the value of pyrolysis oil.

Apart from enhancing pyrolysis reactors and processes to boost the fast pyrolysis oil production rate, upgrading procedures can be accomplished via emulsification, hydrotreating, zeolite upgrading, and supercritical reforming [11,12]. Bio-oil upgrading is most commonly achieved through hydrotreating, which involves hydrodesulfurization (HDS), hydrodenitrogenation (HDN), and hydrodeoxygenation (HDO) reactions [13]. Among these reactions, HDO is an effective method to depolymerize and upgrade lignin and bio-oil, improving the C/O ratio and drawing greater attention [14]. Pyrolysis oil contains a large number of phenolic derivatives, such as phenol, cresol, anisole, and guaiacol, which are used as model compounds in the HDO studies [15,16]. In the HDO reaction, the C-O bond of the model molecule is cleaved to produce saturated or aromatic hydrocarbons [17,18]. In general, HDO of phenolic compounds occurs through two pathways: direct deoxygenation (DDO) and hydrogenation–deoxygenation (HYD) [19]. DDO breaks the C_{Ar}-O bond of phenolic compounds, generating aromatic hydrocarbons. HYD is a continuous process

that involves several steps, including a hydrogenation–dehydration–hydrogenation reaction [20,21]. Furthermore hydrogenolysis, transalkylation, and methanation of the C-C bond can occur simultaneously in the HDO process [22,23].

Methane is a promising clean energy source and can be used as a basic material for advanced chemicals [24–26]. Hydrogenolysis of biomass to methane is a potential energy conversion method. Currently, there are two primary methods of converting biomass to methane-rich gas: biological fermentation and chemical pyrolysis/gasification [27,28]. Biological fermentation typically produces methane with a selectivity of around 45–70%, but it takes a long time and may contain unused lignin residue. In contrast, pyrolysis/gasification is usually carried out at high temperatures (600–1000 °C) and produces a mixture of CH_4, CO_2, etc., with a relatively low CH_4 content [25,29,30]. Therefore, it is essential to design catalysts for converting biomass to methane under mild conditions.

Nickel-based catalysts are promising candidates for converting biomass into biomethane due to their excellent hydrogen dissociation and chemisorption capabilities [31–33]. As an example, in HDO of guaiacol, it is catalyzed using nickel catalysts supported on Al-MCM-41, with lower temperatures favoring the hydrogenation of the aromatic ring and extensive C-C hydrogenolysis occurring at 400 °C [34,35]. In addition, there is a significant increase in methanation activity. The aromatic/cyclohexane hydrogenation and dehydrogenation reactions are thermodynamically sensitive to reaction temperature and pressure due to the complexity of the reaction mechanism. Zhu et al. compare the HDO performances of Ni, Pd, and Pt catalysts without the influence of the solvent and supports [36,37]. Although the HDO activities of Ni are lower than those of Pd and Pt catalysts, the C-C hydrogenolysis reaction of Ni catalysts is more favorable and a large amount of methane is generated [38,39]. This progress demonstrates that Ni-based catalysts are active in C-C hydrogenolysis, methanation, and other reactions in HDO reactions.

This work investigates the influence of temperature on the hydrogenation reaction pathway of nickel catalysts. Anisole was chosen as a representative molecule because it contains a phenyl ring connecting the methoxyl group ($–OCH_3$), one of the major functional groups of the lignin phenolic. Two NiO catalysts are synthesized through the calcination and precipitation methods. The hydrogenation reaction of anisole is examined under identical conditions in a fixed-bed flow reactor at varying temperatures. The selectivity of the catalysts' hydrogenation reactions is significantly different at low temperatures (150 °C), while at 300 °C or higher temperatures, methane is the main product of the hydrogenation of anisole. This finding is important for directly utilizing biomass resources and showing the possibility of producing clean energy.

2. Results and Discussion

In this work, NiO–C is synthesized directly through calcination, and NiO–U is prepared by urea precipitation. The catalytic activity of the catalysts is evaluated through the HDO reaction of anisole. After pretreatment, both nickel catalysts exhibit high conversion under similar reaction conditions, but their selectivity is very different. As shown in Figure 1a, the conversion for C–reduced NiO is approximately 96% at 150 °C, and all of it converts to the hydrogenation product, methoxycyclohexane. Meanwhile, the yield of methoxycyclohexane decreases as temperature increases. The yield of methane gradually rises, suggesting that the hydrogenation of anisole tends to follow the hydrogenolysis route. As displayed in Figure 1b, the products of the reaction of U–reduced NiO are mostly cyclohexane at 150 °C, and the selectivity of methane reaches 100% at 300 °C.

As shown in Figure 1c,d, reaction temperature has a different effect on the three different types of reactions: hydrogenation, HDO, and C-C hydrogenolysis. Firstly, at a low temperature (150 °C), their selectivity is completely different: C–reduced NiO is prone to following the hydrogenation route, while U–reduced NiO is more likely to undergo the HDO reaction. As temperature increases, the hydrogenation reaction of C–reduced NiO and the HDO reaction of U–reduced NiO are obviously inhibited; the reactions of

both catalysts tend to take the C-C hydrogenolysis route. All feedstocks are transformed to methane at a temperature of 300 °C or higher.
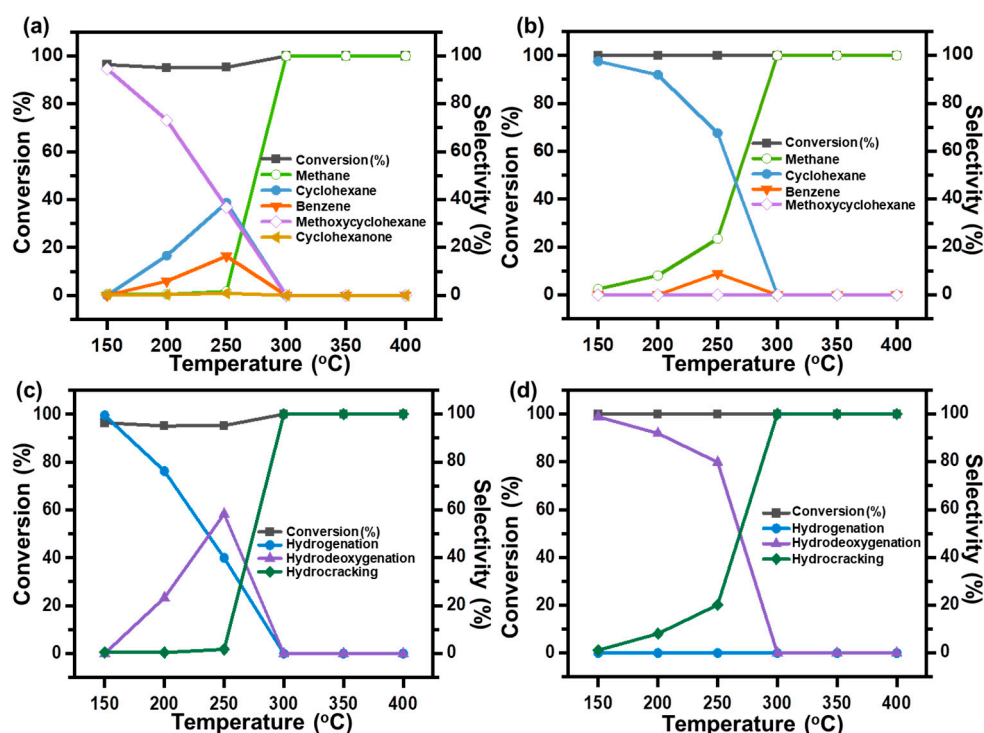

Figure 1. Hydrogenation activity patterns of NiO–C and NiO–U after pretreatment. Conversion of anisole and distribution of products during the reaction as a function of temperature for (**a**) C–reduced NiO and (**b**) U–reduced NiO. Selectivity of hydrogenation products, hydrodeoxygenation products, and hydrocracking products at different temperatures for (**c**) C–reduced NiO and (**d**) U–reduced NiO.

The particle size and morphology of the catalysts after the reactions were studied using scanning electron microscopy (SEM) and transmission electron microscopy (TEM). As shown in Figure 2, a significant difference in particle size and shape between NiO–C catalyst and NiO–U catalyst after the reaction is observed. The morphology results of NiO–C after the reaction (Figure 2a–d) indicate that the spent NiO–C catalyst exists in the form of larger particles compared to those of the spent NiO–U catalyst. As exhibited in Figure 2e–h, it can be seen that the particles of NiO–U are irregularly distributed after the reaction, and thus generate more stacked pore structures. Furthermore, in the high-resolution TEM image (Figure 2h), the lattice spacing of the spent NiO–U catalyst is 0.20 nm, which corresponds to the (111) plane of metal Ni. This result matches the XRD patterns, as shown in Figure 3 [40].

The crystalline structures of fresh catalysts were examined. The fresh catalysts both exhibit the same diffraction peaks, which are assigned to NiO (PDF#47-1049), as shown in Figure 3a [32]. Moreover, the XRD pattern of NiO–C has a narrower peak width and higher peak intensity compared to NiO–U, indicating significant differences in the degree of crystallization and particle size between the two catalysts. NiO–C exhibits better crystallinity as compared to NiO–U. The particle sizes of the catalysts were calculated by the Scherrer formula and are shown in Table 1 [41]. It can be inferred that the crystal size of NiO–C is larger than that of NiO–U. The structure of the catalysts after pretreatment and reaction are further evaluated (Figure 3b), reveals that both catalysts are reduced to nickel (PDF#04-0850). The reduced and spent catalysts exhibit similar crystallinity and particle size [42].
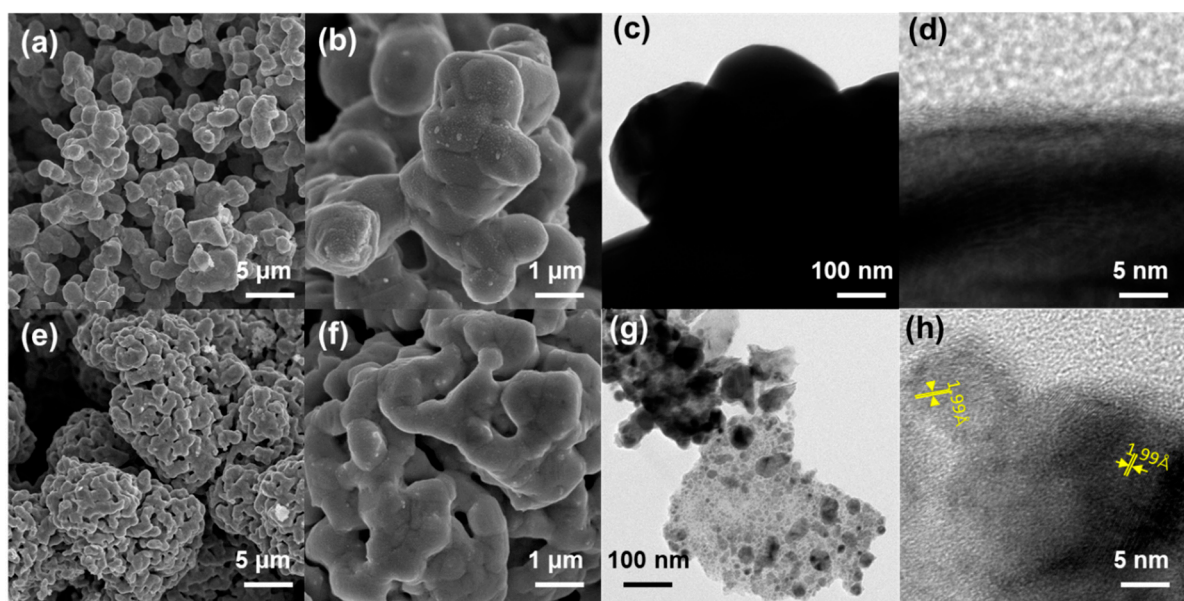
Figure 2. Scanning electron microscope (SEM) and transmission electron microscope (TEM) images of NiO–C and NiO–U: SEM images of (**a**,**b**) NiO–C and (**e**,**f**) NiO–U; TEM images of (**c**,**d**) NiO–C and (**g**,**h**) NiO–U.
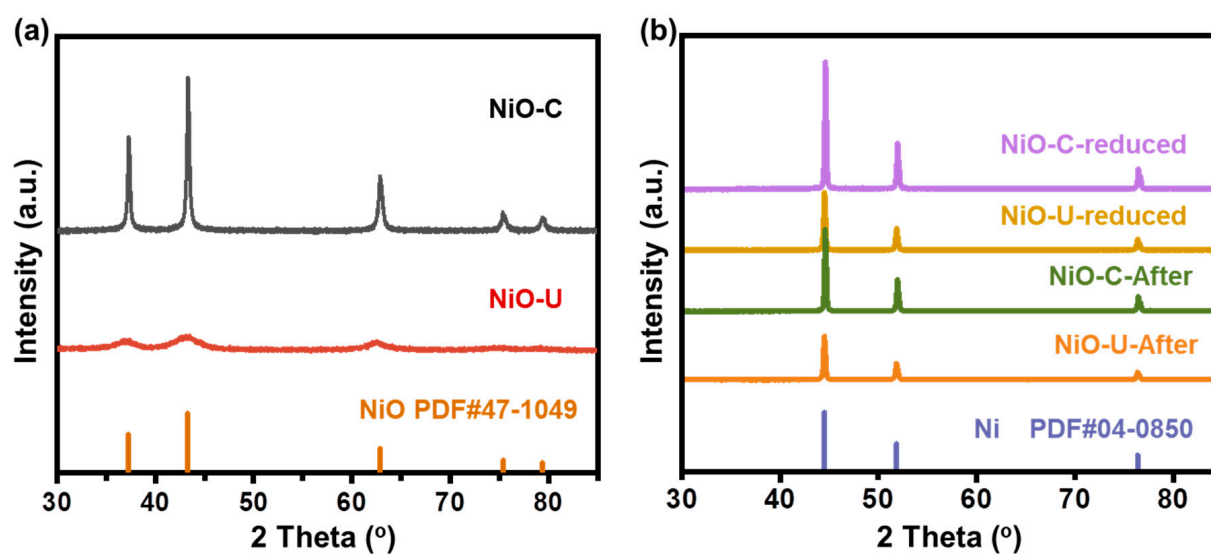

Figure 3. X-ray diffraction patterns of NiO–C and NiO–U. (**a**) Fresh NiO–C and NiO–U; the JCPDF reference is PDF#47-1049 for NiO. (**b**) Catalysts after pretreatment and reaction; the JCPDF reference is PDF#04-0850.

Table 1. XRD peak analyses of fresh, reduced, and spent NiO–C and NiO–U catalysts.

Sample	Miller Indices (hkl) Plane	2-Theta (°)	FWHM (Rad)	Crystallite Size (nm) [a]
NiO–C	(200)	43.3	0.28	33
NiO–U	(200)	43.1	3.16	3
NiO–C–reduced	(111)	44.6	0.18	53
NiO–U–reduced	(111)	44.5	0.20	47
NiO–C–after	(111)	44.6	0.18	53
NiO–U–after	(111)	44.5	0.20	47

[a] Average sizes were estimated using the Scherrer formula.

Raman spectra were used to investigate the metal state and structures of the fresh catalysts. As presented in Figure 4, it was found that the two NiO catalysts have similar Raman spectra. For NiO–U, the spectra show signal peaks at 345 cm^{-1}, 500 cm^{-1}, and 1066 cm^{-1}, which correspond to the first-order phonon TO, the first-order phonon LO, and the second-order phonon 2LO of NiO crystals [43,44]. The existence of 1TO and 1LO modes in the Raman spectra suggests that Ni^{2+} and disordered oxygen may be present. This conclusion suggests that the catalysts are NiO materials, which is in agreement with the XRD (Figure 3) results. Similarly, for NiO–C, the peaks at 500 cm^{-1} and 1066 cm^{-1} correspond to the 1TO and 2LO signals of nickel oxide crystals. Combined with the above characterization data, the two catalysts are nickel oxide crystals before pretreatment.
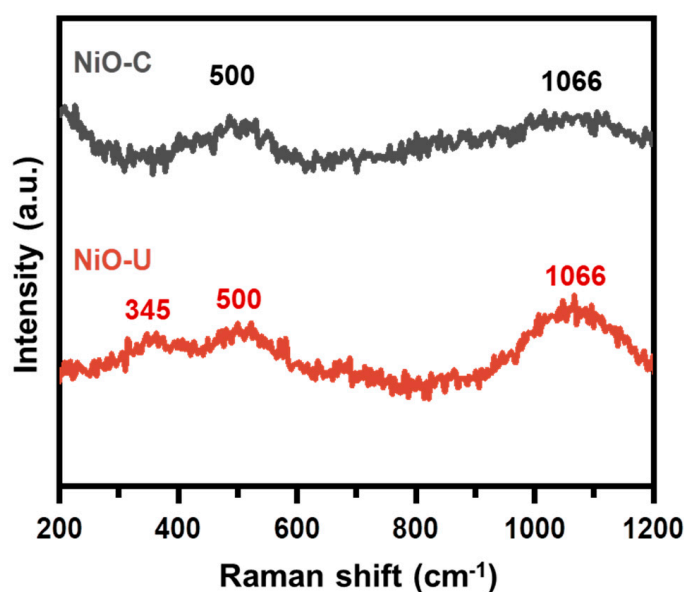

Figure 4. Raman spectra of fresh NiO–C and NiO–U catalysts.

The redox properties of the catalysts were further investigated using temperature-programmed reduction (TPR), as shown in Figure 5. It can be observed that the reduction peaks of the two catalysts are both lower than 400 °C, indicating that NiO–C and NiO–U can be fully reduced at 400 °C. NiO–C displays a wide H_2 reduction peak at 360 °C, which is assigned to the reduction of NiO [42,45]. NiO–U exhibits three narrow H_2 reduction peaks at 233 °C, 261 °C, and 283 °C, which are lower than those observed in NiO–C. A temperature of 200–300 °C is related to the phase transition and reduction of NiO. NiO–U can be reduced to nickel monomers at 350 °C [46].

Surface elemental composition and valence of elements in NiO catalysts were analyzed through XPS spectra. Figure 6a shows the XPS spectra of NiO–C catalysts, including a fresh catalyst, pretreated catalyst, and spent catalyst. The fresh NiO–C catalyst shows two peaks at 853.7 and 855.3 eV, which are related to Ni^{2+} and Ni^{3+} ions, respectively. And the peak at 860.7 eV is attributed to a high-spin Ni $2p3/2$ satellite [47,48]. It is worth noting that the existence of Ni^{3+} does not necessarily indicate the presence of Ni_2O_3 in the sample. According to other research, it has been reported that Ni^{2+} in NiO is more likely to generate defects, leading to the loss of an electron by the two neighboring Ni^{2+} and the production of Ni^{3+} on the NiO surface to preserve the charge balance [49].

The NiO–C catalyst after pretreatment was also evaluated, as shown in Figure 6a. Compared to fresh NiO–C, it can be observed that the intensity of the Ni^{2+} peak weakened and a new peak appeared at 852.4 eV, which corresponds to Ni^0 [50,51]. This indicates that nickel oxide is partially reduced to nickel monomers. After the HDO reaction, the catalyst also has a high peak at 852.4 eV, suggesting that nickel monomers are present in the catalyst. However, Ni^{3+} is still present in spent catalysts, which may be due to the oxidation of the catalysts by exposure to air after the reaction (Figure 6a). [32,52] Combined with the results

of the XRD (Figure 3) and H$_2$-TPR (Figure 5) data, it can be assumed that metallic nickel is the main active phase in the reaction.
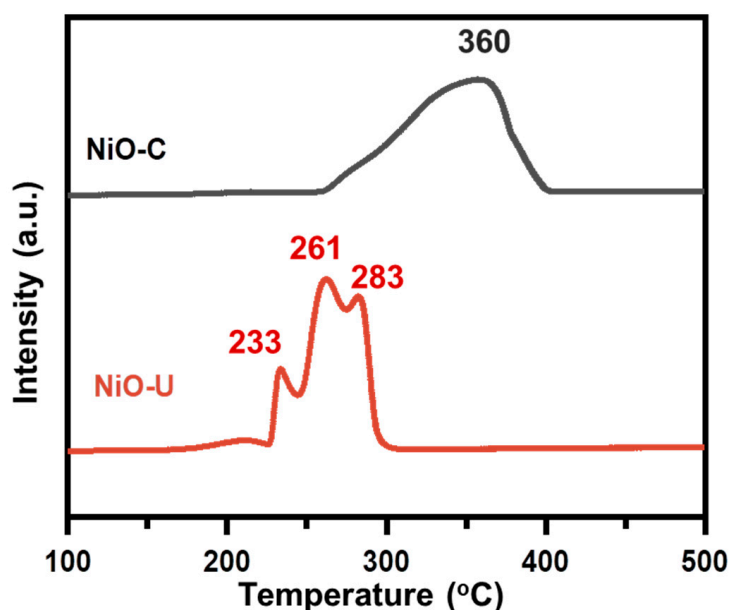

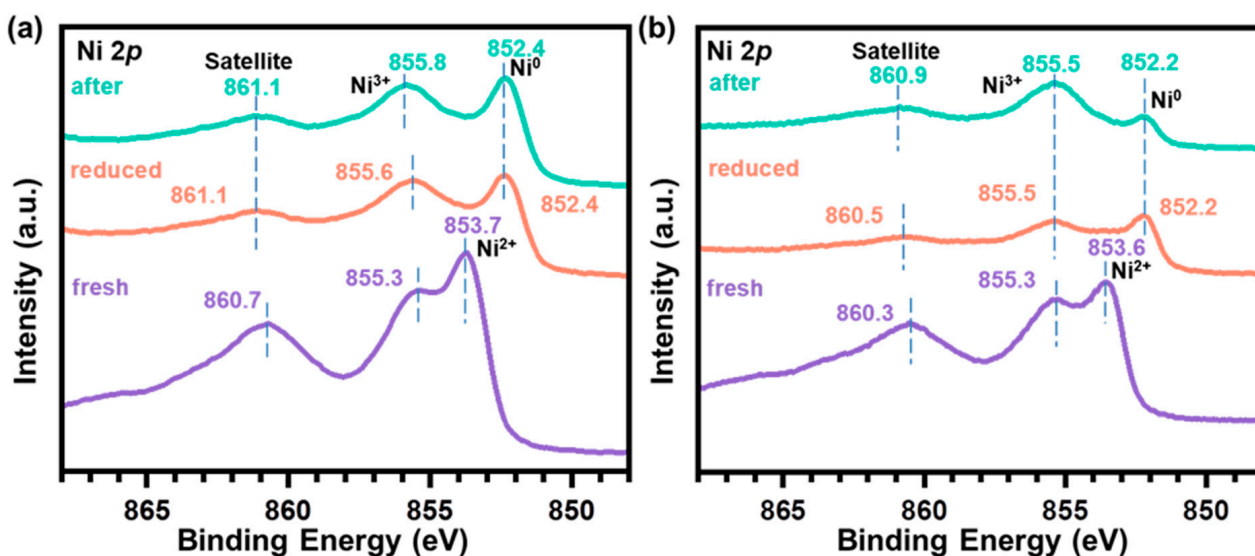**Figure 5.** Temperature-programmed reduction (H$_2$-TPR) of fresh NiO–C and fresh NiO–U.

Figure 6. X-ray photoelectron spectra of Ni 2*p* for (**a**) NiO–C and (**b**) NiO–U catalysts before the reaction, after pretreatment, and after the reaction.

NiO–U and NiO–C have remarkably similar profiles and catalyst valence transformations. According to Figure 6b, Ni^{2+} and Ni^{3+} peaks in the fresh NiO–U catalyst are located at 853.6 eV and 855.3 eV, respectively. The Ni 2*p* spectra of NiO–U undergo the same changes as those of NiO–C during pretreatment and the reaction. A Ni^0 peak appears, suggesting that reduced and spent catalysts are converted to monomeric nickel. Metal Ni undergoes spontaneous oxidation in the atmosphere, and then the presence of Ni^{3+} is captured by XPS.

Figure 7 shows the XPS spectra of O 1*s* for fresh, reduced and spent the NiO–C and NiO–U catalysts. The peaks at 529, 530.6, and 532 eV in fresh NiO–C are attributed to lattice oxygen, disordered oxygen, and surface-adsorbed hydroxyl group, respectively. According to the changes in the peak positions and peak intensities of O 1*s*, it can be seen

that the fresh catalyst has a higher lattice oxygen content [53]. However, as the catalyst is gradually reduced, nickel oxide gradually turns into nickel, reducing lattice oxygen content while gradually increasing the content of disordered oxygen. Table 2 lists the changes and proportions of various oxygen types in NiO. The trends in the positions and intensities of the peaks on the plots of O 1*s* for NiO–U catalysts are similar to those of NiO–C catalysts, but there is a significant difference in the amount of the various oxygen species present. In U–reduced NiO, disordered oxygen (530.9 eV) increases significantly to 77.5% (531 eV) after the reaction, which is nearly twice as much as that in NiO–C. Therefore, the amount of disordered oxygen may influence catalyst selectivity in low-temperature reactions [51,54].
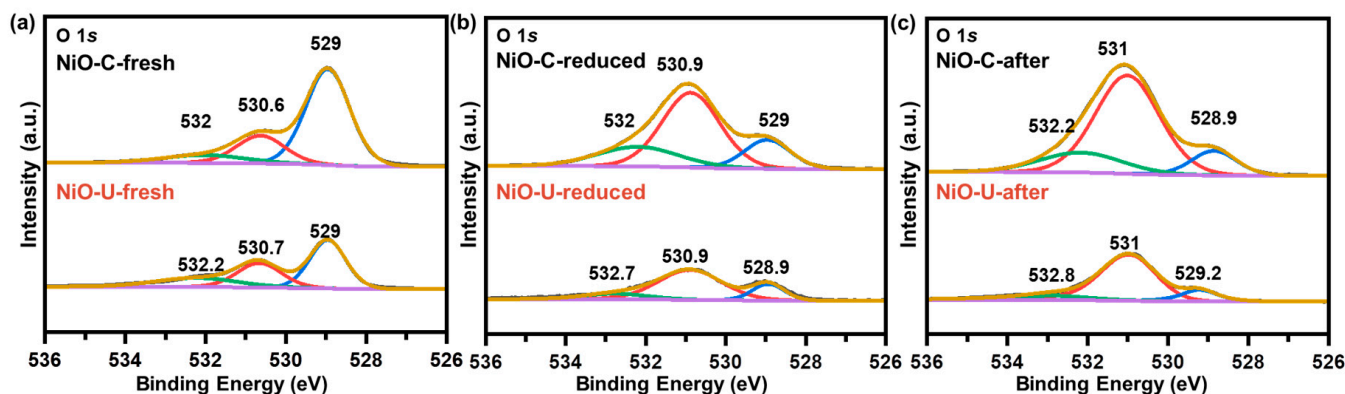

Figure 7. X-ray photoelectron spectroscopy (XPS) spectra of O 1*s* for NiO–C and NiO–U catalysts (**a**) before the reaction, (**b**) after reduction, and (**c**) after the reaction. The blue line represents lattice oxygen, red line is disordered oxygen and green line is hydroxyl oxygen.

Table 2. Fresh catalysts, reduced catalysts, and spent NiO–C and NiO–U catalysts with different oxygen ratios.

Sample	Oxygen Species	Fresh	Reduced	After
NiO–C	lattice oxygen (%)	42.3	30.0	22.4
	disordered oxygen (%)	38.9	33.8	44.3
	hydroxyl oxygen (%)	18.8	36.2	33.3
NiO–U	lattice oxygen (%)	48,8	19.0	13.1
	disordered oxygen (%)	30.3	67.8	77.5
	hydroxyl oxygen (%)	20.9	13.2	9.4

The surface characteristics of NiO catalysts were investigated and analyzed by DRIFT-CO. Before the tests, two catalysts were pretreated with pure H_2 (16 mL/min) at 350 °C for 1 h in situ cell. For C–reduced NiO, two peaks at 2100–2200 cm^{-1}, assigned to the gas phase of CO, are observed, as seen in Figure 8a. This indicates that there is no chemical adsorption of CO on the surface of C–reduced NiO. The NiO–U catalyst after pretreatment undergoes the same testing procedure as the NiO–C. In contrast, U–reduced NiO shows two additional peaks at 2050 and 1975 cm^{-1}, which are related to linear and bridge CO adsorbed on metallic nickel (Figure 8b) [55]. Following argon purging, the adsorption peaks' strength gradually decreases, and within 30 min, they completely disappear.

The absorption and desorption of H_2O on NiO–U were also tested. As shown in Figure 9a, when water vapor is bubbled into the in situ cell at 300 °C, there is a broad absorption band at 3500–4000 cm^{-1}, which is attributed to the O-H stretching vibration. This could be caused by the water molecules adsorbed on the surface of NiO. When the bubbling stops, the peak of the O-H stretching vibration gradually decreases, indicating that the peak is mainly caused by physically adsorbed H_2O. In addition, a weak absorption band is produced near 1650 cm^{-1} due to the effect of adsorbed H_2O, which is attributed to the H-O-H bending vibration mode [56]. The sharp peaks near 1320 and 3015 cm^{-1} are

assigned to gaseous methane, proving that methane is produced. This is a result of the presence of contaminated carbon in the catalyst, which may have reacted with H_2 at 300 °C. This confirms that the C from the C-C cleavage of anisole can react with H_2 to produce methane, suggesting that the HDO reaction of anisole at 300 °C and above is primarily focused on hydrogenolysis.
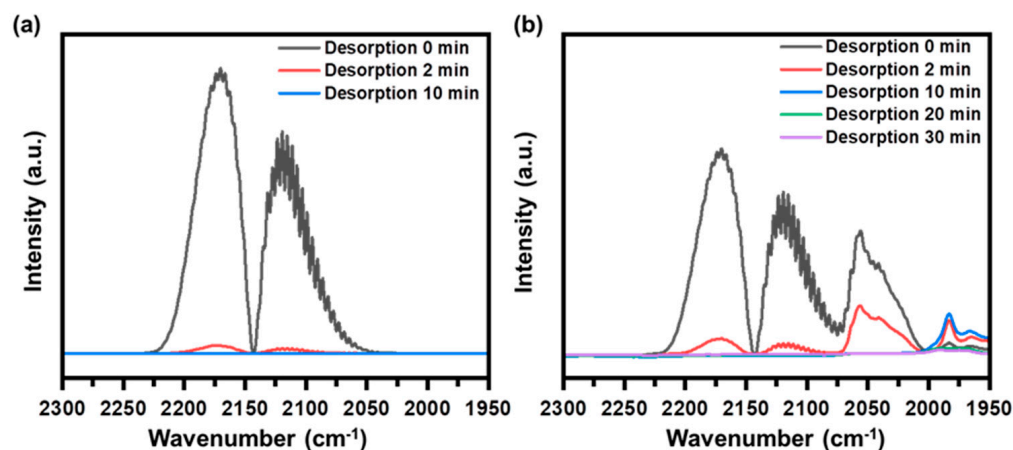

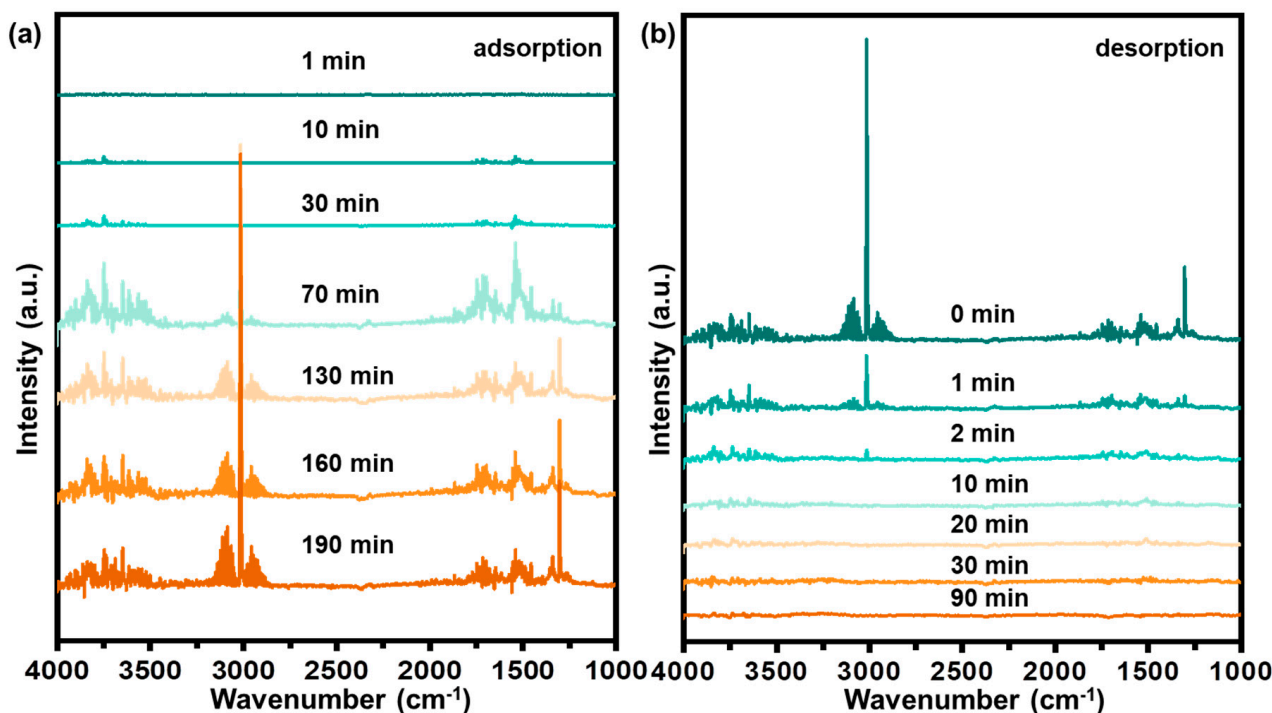**Figure 8.** DRIFT-CO spectra of (**a**) NiO–C and (**b**) NiO–U catalysts.

Figure 9. DRIFT-H_2O spectra of NiO–U catalysts. (**a**) is the adsorption of water by NiO over 190 min, and (**b**) is the desorption of H_2O when NiO–U stops bubbling water vapor and purges with pure Ar (20 mL/min).

3. Experimental Methods

3.1. Synthesis of Catalysts

NiO–C was obtained by calcinating 3 g $Ni(NO_3)_2 \cdot 6H_2O$ (AR, Aladdin, Shanghai, China) in a muffle furnace at 350 °C for 3 h at a heating rate of 5 °C/min. NiO–U was prepared by the precipitation method. First of all, 7.793 g of $Ni(NO_3)_2 \cdot 6H_2O$ (AR, Aladdin, Shanghai, China) and 19.31 g of urea (AR, Aladdin, Shanghai, China) were dissolved in 200 mL of deionized water, then heated to 80 °C and stirred for 3 h with a rate of 400 r/min.

Then, the solution was cooled to room temperature and filtered. Finally, the product of the precipitate was filtered and dried at 80 °C for 12 h. Then, the catalyst was calcined at 350 °C in air for 3 h, and NiO–U was obtained.

3.2. Characterization Method

Scanning electron microscopy (SEM): Surface morphology of the samples was analyzed using a Regulus 8100 Scanning electron microscope made by Hitachi Company (Tokyo, Japan). The scan acceleration voltage was 0.5–30 kV. Before the test, a small amount of the sample was smeared on a conductive adhesive, and the unattached catalyst powder was blown off by a rubber suction bulb.

Transmission electron microscopy (TEM): TEM studies of the samples were performed using a TALOS F200s G2 field emission TEM (FEI, Hillsboro, OR, USA, accelerating voltage of 200 kV) to determine the morphology, metal distribution, particle size, and lattice fringes of the catalysts. In a typical TEM sample preparation, 10 mg of the sample was ground to a fine powder and dispersed in 5 mL of anhydrous ethanol by ultrasound. After dispersing the sample, the ethanol solution was added dropwise to the copper grid with a carbon lacey film. The sample was sent to be tested after being dried naturally. The morphologies of the samples were obtained in TEM and HRTEM modes.

X-ray powder diffraction (XRD): XRD patterns were measured by a Rigaku Smart Lab SE diffractometer (Rigaku, Tokyo, Japan) with copper Kα irradiation (λ = 0.1540 nm). The scan range was 30–85°. The scan rate was 10°/min.

H_2 temperature-programmed reduction (H_2-TPR): The reducibility of the catalysts was tested by H_2-TPR. Temperature programming curves were recorded in an Auto-Chem II instrument (Micromeritics Instrument Corporation, Norcross, GA, USA) equipped with a TCD detector. During the test, 0.1 g fresh catalyst was loaded into a quartz tube reactor and then pretreated at 300 °C in a He gas environment for 60 min before cooling to 30 °C. In the temperature-programmed test, the temperature was raised to 500 °C at a heating rate of 10 °C/min in 10% H_2/Ar gas mixture.

X-ray photoelectron spectroscopy (XPS): XPS spectra were measured with an ES-CALAB 250XI spectrometer (Thermo-Fisher, Waltham, MA, USA). Al target (1486.6 eV) was used as the source of X-ray excitation, and C1 at 284.6 eV was used for charge correction. The XPS spectra were analyzed and fitted using Advantage software.

Diffuse reflectance infrared Fourier transform spectra of CO/H_2O (DRIFT-CO/H_2O): CO and H_2O adsorption on the catalyst surface was detected by DRIFT-CO and DRIFT-H_2O. Experiments were performed on a Nicolet IS50 FTIR spectrometer (Thermo Fisher Scientific, Waltham, MA, USA) with a ZnSe window and an MCT detector. A certain amount of NiO catalyst was reduced with 10% H_2/Ar (20 mL/min) and pure Ar (20 mL/min) for 1 h at 350 °C. Then, it was naturally cooled to room temperature or 300 °C in a reduced atmosphere and swept with pure Ar (20 mL/min) until there was no H_2 in the pipe. When the OMNIC spectra software detected that the baseline was stable, 10% CO/Ar or H_2O was introduced to the sample cell and the spectra for testing. When CO or H_2O was saturated, the gas path was closed, and infrared desorption spectra were recorded.

Raman: Raman spectroscopy (Raman) was used to measure the state and structure of catalyst metals. Tests were performed on a DXR2xi Micro Raman Spectrometer (Thermo Fisher Scientific, Waltham, MA, USA) with a 532 nm laser source. During the test, laser intensity and exposure time were adjusted to look for a better signal-to-noise ratio and obtain clear Raman images.

3.3. Catalyst Evaluation

The catalytic reaction was carried out in a fixed-bed reactor with 100 mg NiO–C or 100 mg NiO–U catalyst and a certain amount of quartz sand in a quartz tube. The catalysts were pretreated with H_2 (16 mL/min) at 350 °C for 1 h. After pretreatment, the reactor was cooled to room temperature naturally, and then the gas path was changed so that H_2 (4 mL/min) passed through the anisole bubbling bottle and the anisole vapor was carried

into the reactor. The reactor heating rate was 10 mL/min, and the catalytic performance of the catalysts was evaluated at temperatures from 150 to 400 °C. During the reaction, the gas flowing out of the reactor was detected by online GC in real time, and the conversion and selectivity for each product were calculated as follows.

$$\text{Conversion}_{\text{anisole}}\ (\%) = \frac{N_{\text{anisole,in}} - N_{\text{anisole,out}}}{N_{\text{anisole,in}}} \times 100\%$$

$\text{Conversion}_{\text{anisole}}$ (%)—conversion of anisole; $N_{\text{anisole,in}}$—mol of anisole in pristine mixed gas; $N_{\text{anisole,out}}$—mol of anisole in exit gas.

$$\text{Selectivity}_{\text{X}}\ (\%) = \frac{N_{\text{X}}}{\sum N_{\text{All, products}}} \times 100\%$$

$\text{Selectivity}_{\text{X}}$—selectivity of X product; N_{X}—mol of product X; $\sum N_{\text{All,products}}$—sum mol of all products.

$$\text{Selectivity}_{\text{HDO}}(\%) = \frac{\sum N_{\text{HDO}}}{N_{\text{anisole,in}} - N_{\text{anisole,out}}} \times 100\%$$

$\text{Selectivity}_{\text{HDO}}$—selectivity of hydrodeoxygenation products; $\sum N_{\text{HDO}}$—sum mol of HDO products.

$$\text{Selectivity}_{\text{Hydrogenation}}\ (\%) = \frac{\sum N_{\text{Hydrogenation}}}{N_{\text{anisole,in}} - N_{\text{anisole,out}}} \times 100\%$$

$\text{Selectivity}_{\text{Hydrogenation}}$—selectivity of hydrogenation products; $\sum N_{\text{Hydrogenation}}$—sum mol of hydrogenation products.

$$\text{Selectivity}_{\text{Hydrocracking}}\ (\%) = \frac{\sum N_{\text{Hydrocracking}}}{N_{\text{anisole,in}} - N_{\text{anisole,out}}} \times 100\%$$

$\text{Selectivity}_{\text{Hydrocracking}}$—selectivity of cracking products; $\sum N_{\text{Hydrocracking}}$—sum mol of cracking products, which is methane in this work.

4. Conclusions

In summary, two NiO catalysts were prepared by different methods and used for the reaction of anisole hydrodeoxygenation. After pretreatment, it was found that the two catalysts have completely different selectivity for HDO under low temperature conditions (150 °C). The two catalysts were characterized by XRD, TEM, and Raman, which found that fresh catalysts are nickel oxides. After the HDO reaction, nickel catalysts transform into metallic nickel, which was confirmed by XRD, TEM and XPS analysis. According to the H_2-TPR results, NiO–U is completely reduced at a lower temperature. In addition, the DRIFT-H_2O results revealed that the HDO reaction of anisole with U–reduced NiO catalyst tends to follow the hydrogenolysis pathway at 300 °C, and its selectivity to methane is nearly 100%. The catalytic performance and characterization results indicate that the three different types of route—anisole hydrogenation, HDO, and C-C hydrogenolysis—are all affected by temperature. As shown in Scheme 1, at 150 °C, C-reduced NiO is prone to following the hydrogenation route, and U-reduced NiO is more likely to undergo the HDO reaction. When temperature increases to 300 °C, the reaction will undergo C-C hydrogenolysis. This work provides a new insight into the hydrodeoxygenation of anisole.
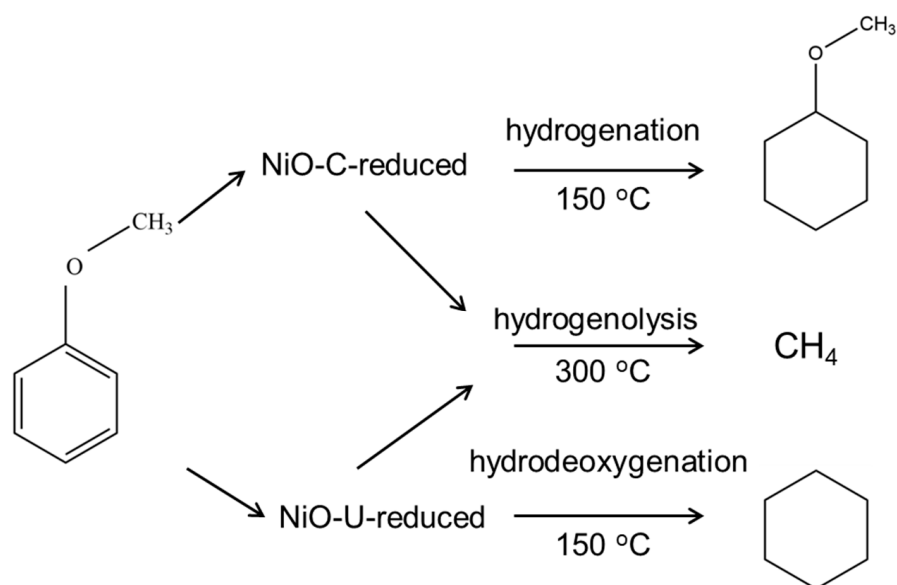
Scheme 1. Scheme of the transformations of anisole under different temperatures with C–reduced NiO and U–reduced NiO.

Author Contributions: S.Z.: Investigation, Formal analysis, Writing—Original Draft; X.L.: Investigation, Formal analysis; Y.X.: Investigation, Writing—Review and Editing; Y.T.: Conceptualization, Writing—Review and Editing, Supervision. All authors have read and agreed to the published version of the manuscript.

Data Availability Statement: The data are available upon reasonable request.

References

1. Dresselhaus, M.S.; Thomas, I.L. Alternative energy technologies. *Nature* **2001**, *414*, 332–337. [CrossRef] [PubMed]
2. Guo, X.; Fang, G.; Li, G.; Ma, H.; Fan, H.; Yu, L.; Ma, C.; Wu, X.; Deng, D.; Wei, M.; et al. Direct, Nonoxidative Conversion of Methane to Ethylene, Aromatics, and Hydrogen. *Science* **2014**, *344*, 616–619. [CrossRef]
3. Huber, G.W.; Iborra, S.; Corma, A. Synthesis of Transportation Fuels from Biomass: Chemistry, Catalysts, and Engineering. *Chem. Rev.* **2006**, *106*, 4044–4098. [CrossRef] [PubMed]
4. de Lasa, H.; Salaices, E.; Mazumder, J.; Lucky, R. Catalytic Steam Gasification of Biomass: Catalysts, Thermodynamics and Kinetics. *Chem. Rev.* **2011**, *111*, 5404–5433. [CrossRef] [PubMed]
5. Xu, H.; Li, H. Regulating the crystal phase of Pd/Nb_2O_5 for vanillin selective HDO at room temperature. *J. Catal.* **2023**, *423*, 105–117. [CrossRef]
6. Rajendran, A.; Cui, T.-y.; Fan, H.-x.; Yang, Z.-f.; Feng, J.; Li, W.-y. A comprehensive review on oxidative desulfurization catalysts targeting clean energy and environment. *J. Mater. Chem. A* **2020**, *8*, 2246–2285. [CrossRef]
7. López-Benítez, A.; Berhault, G.; Burel, L.; Guevara-Lara, A. Novel NiW hydrodesulfurization catalysts supported on Sol-Gel $Mn-Al_2O_3$. *J. Catal.* **2017**, *354*, 197–212. [CrossRef]
8. Albersberger, S.; Hein, J.; Schreiber, M.W.; Guerra, S.; Han, J.; Gutiérrez, O.Y.; Lercher, J.A. Simultaneous hydrodenitrogenation and hydrodesulfurization on unsupported Ni-Mo-W sulfides. *Catal. Today* **2017**, *297*, 344–355. [CrossRef]
9. Hosseinpour, M.; Golzary, A.; Saber, M.; Yoshikawa, K. Denitrogenation of biocrude oil from algal biomass in high temperature water and formic acid mixture over H+ZSM-5 nanocatalyst. *Fuel* **2017**, *206*, 628–637. [CrossRef]
10. Pinheiro, A.; Hudebine, D.; Dupassieux, N.; Geantet, C. Impact of Oxygenated Compounds from Lignocellulosic Biomass Pyrolysis Oils on Gas Oil Hydrotreatment. *Energy Fuels* **2009**, *23*, 1007–1014. [CrossRef]
11. Yu, X.; Williams, C.T. Recent applications of nickel and nickel-based bimetallic catalysts for hydrodeoxygenation of biomass-derived oxygenates to fuels. *Catal. Sci. Technol.* **2023**, *13*, 802–825. [CrossRef]
12. Chheda, J.N.; Huber, G.W.; Dumesic, J.A. Liquid-Phase Catalytic Processing of Biomass-Derived Oxygenated Hydrocarbons to Fuels and Chemicals. *Angew. Chem. Int. Ed.* **2007**, *46*, 7164–7183. [CrossRef] [PubMed]
13. Furimsky, E. Catalytic hydrodeoxygenation. *Appl. Catal. A Gen.* **2000**, *199*, 147–190. [CrossRef]

14. Li, H.; Ma, H.; Zhao, W.; Li, X.; Long, J. Upgrading lignin bio-oil for oxygen-containing fuel production using Ni/MgO: Effect of the catalyst calcination temperature. *Appl. Energy* **2019**, *253*, 113613. [CrossRef]

15. Zhu, X.; Lobban, L.L.; Mallinson, R.G.; Resasco, D.E. Bifunctional transalkylation and hydrodeoxygenation of anisole over a Pt/HBeta catalyst. *J. Catal.* **2011**, *281*, 21–29. [CrossRef]

16. Yang, Y.; Ochoa-Hernández, C.; de la Peña O'Shea, V.; Pizarro, P.; Coronado, J.M.; Serrano, D.P. Effect of metal–support interaction on the selective hydrodeoxygenation of anisole to aromatics over Ni-based catalysts. *Appl. Catal. B Environ.* **2014**, *145*, 91–100. [CrossRef]

17. Zhang, S.; Liu, X.; Lin, H.; Chen, R.; Chen, Y.; Xu, Y.; Xu, K.; Zhao, H.; Tan, L.; Wu, L.; et al. Unveiling the in-situ formation of single-atomically dispersed Pd-Fe bimetallic catalytic sites during anisole hydrodeoxygenation. *Mol. Catal.* **2023**, *547*, 113401. [CrossRef]

18. Strapasson, G.B.; Sousa, L.S.; Báfero, G.B.; Leite, D.S.; Moreno, B.D.; Rodella, C.B.; Zanchet, D. Acidity modulation of Pt-supported catalyst enhances C-O bond cleavage over acetone hydrodeoxygenation. *Appl. Catal. B Environ.* **2023**, *335*, 122863. [CrossRef]

19. Prabhudesai, V.S.; Gurrala, L.; Vinu, R. Catalytic Hydrodeoxygenation of Lignin-Derived Oxygenates: Catalysis, Mechanism, and Effect of Process Conditions. *Energy Fuels* **2021**, *36*, 1155–1188. [CrossRef]

20. Zhang, J.; Sun, J.; Wang, Y. Recent advances in the selective catalytic hydrodeoxygenation of lignin-derived oxygenates to arenes. *Green Chem.* **2020**, *22*, 1072–1098. [CrossRef]

21. Lup, A.N.K.; Abnisa, F.; Daud, W.M.A.W.; Aroua, M.K. A review on reaction mechanisms of metal-catalyzed deoxygenation process in bio-oil model compounds. *Appl. Catal. A Gen.* **2017**, *541*, 87–106. [CrossRef]

22. Zheng, Y.; Zhao, N.; Chen, J. Enhanced direct deoxygenation of anisole to benzene on SiO2-supported Ni-Ga alloy and intermetallic compound. *Appl. Catal. B Environ.* **2019**, *250*, 280–291. [CrossRef]

23. Liu, X.; Zhang, S.; Zhao, H.; Lin, H.; Xu, K.; Xu, Y.; Tan, L.; Wu, L.; Tang, Y. In-situ studies on the synergistic effect of Pd-Mo bimetallic catalyst for anisole hydrodeoxygenation. *Mol. Catal.* **2022**, *530*, 112591. [CrossRef]

24. Zhou, H.; Wang, M.; Wang, F. Oxygen-vacancy-mediated catalytic methanation of lignocellulose at temperatures below 200 °C. *Joule* **2021**, *5*, 3031–3044. [CrossRef]

25. Si, X.; Lu, R.; Zhao, Z.; Yang, X.; Wang, F.; Jiang, H.; Luo, X.; Wang, A.; Feng, Z.; Xu, J.; et al. Catalytic production of low-carbon footprint sustainable natural gas. *Nat. Commun.* **2022**, *13*, 258. [CrossRef] [PubMed]

26. Xu, Y.; An, Z.; Yu, X.; Yao, J.; Lv, Q.; Yang, H.; Lv, Z.; Guo, H.; Jiang, Q.; Liu, W.; et al. Enhanced catalytic stability and structural evolution of Rh-BN interface in dry reforming of methane under intensified CO$_2$ partial pressure. *J. Catal.* **2023**, *427*, 115094. [CrossRef]

27. Ghimire, N.; Bakke, R.; Bergland, W.H. Liquefaction of lignocellulosic biomass for methane production: A review. *Bioresour. Technol.* **2021**, *332*, 125068. [CrossRef] [PubMed]

28. Wang, Z.; Peng, X.; Xia, A.; Shah, A.A.; Yan, H.; Huang, Y.; Zhu, X.; Zhu, X.; Liao, Q. Comparison of machine learning methods for predicting the methane production from anaerobic digestion of lignocellulosic biomass. *Energy* **2023**, *263*, 125883. [CrossRef]

29. Ren, Z.; Si, X.; Chen, J.; Li, X.; Lu, F. Catalytic Complete Cleavage of C–O and C–C Bonds in Biomass to Natural Gas over Ru(0). *ACS Catal.* **2022**, *12*, 5549–5558. [CrossRef]

30. Gassner, M.; Maréchal, F. Thermo-economic optimisation of the polygeneration of synthetic natural gas (SNG), power and heat from lignocellulosic biomass by gasification and methanation. *Energy Environ. Sci.* **2012**, *5*, 5768–5789. [CrossRef]

31. Xie, J.; Xi, Y.; Gao, W.; Zhang, H.; Wu, Y.; Zhang, R.; Yang, H.; Peng, Y.; Li, F.; Li, Z.; et al. Hydrogenolysis of Lignin Model Compounds on Ni Nanoparticles Surrounding the Oxygen Vacancy of CeO$_2$. *ACS Catal.* **2023**, *13*, 9577–9587. [CrossRef]

32. Teles, C.A.; Ciotonea, C.; Le Valant, A.; Canaff, C.; Dhainaut, J.; Clacens, J.-M.; Noronha, F.B.; Richard, F.; Royer, S. Optimization of catalyst activity and stability in the m-cresol hydrodeoxygenation through Ni particle size control. *Appl. Catal. B Environ.* **2023**, *338*, 123030. [CrossRef]

33. Stanley, J.T.; Thanarasu, A.; Kumar, P.S.; Periyasamy, K.; Raghunandhakumar, S.; Periyaraman, P.; Devaraj, K.; Dhanasekaran, A.; Subramanian, S. Potential pre-treatment of lignocellulosic biomass for the enhancement of biomethane production through anaerobic digestion—A review. *Fuel* **2022**, *318*, 123593. [CrossRef]

34. Taghvaei, H.; Moaddeli, A.; Khalafi-Nezhad, A.; Iulianelli, A. Catalytic hydrodeoxygenation of lignin pyrolytic-oil over Ni catalysts supported on spherical Al-MCM-41 nanoparticles: Effect of Si/Al ratio and Ni loading. *Fuel* **2021**, *293*, 120493. [CrossRef]

35. Lu, X.; Guo, H.; Chen, J.; Wang, D.; Lee, A.F.; Gu, X. Selective Catalytic Transfer Hydrogenation of Lignin to Alkyl Guaiacols Over NiMo/Al-MCM-41. *ChemSusChem* **2022**, *15*, e202200099. [CrossRef] [PubMed]

36. Wu, X.; Liu, C.-J.; Wang, H.; Ge, Q.; Zhu, X. Origin of strong metal-support interactions between Pt and anatase TiO$_2$ facets for hydrodeoxygenation of m-cresol on Pt/TiO$_2$ catalysts. *J. Catal.* **2023**, *418*, 203–215. [CrossRef]

37. Cui, B.; Wang, H.; Han, J.; Ge, Q.; Zhu, X. Crystal-phase-depended strong metal-support interactions enhancing hydrodeoxygenation of m-cresol on Ni/TiO$_2$ catalysts. *J. Catal.* **2022**, *413*, 880–890. [CrossRef]

38. Chen, C.; Chen, G.; Yang, F.; Wang, H.; Han, J.; Ge, Q.; Zhu, X. Vapor phase hydrodeoxygenation and hydrogenation of m-cresol on silica supported Ni, Pd and Pt catalysts. *Chem. Eng. Sci.* **2015**, *135*, 145–154. [CrossRef]

39. Fang, W.; Liu, S.; Steffensen, A.K.; Schill, L.; Kastlunger, G.; Riisager, A. On the Role of Cu$^+$ and CuNi Alloy Phases in Mesoporous CuNi Catalyst for Furfural Hydrogenation. *ACS Catal.* **2023**, *13*, 8437–8444. [CrossRef]

40. He, L.; Li, M.; Li, W.-C.; Xu, W.; Wang, Y.; Wang, Y.-B.; Shen, W.; Lu, A.-H. Robust and Coke-free Ni Catalyst Stabilized by 1–2 nm-Thick Multielement Oxide for Methane Dry Reforming. *ACS Catal.* **2021**, *11*, 12409–12416. [CrossRef]

41. Lu, S.; Yang, H.; Zhou, Z.; Zhong, L.; Li, S.; Gao, P.; Sun, Y. Effect of In_2O_3 particle size on CO_2 hydrogenation to lower olefins over bifunctional catalysts. *Chin. J. Catal.* **2021**, *42*, 2038–2048. [CrossRef]

42. Wang, X.; Chen, J. Effects of indium on Ni/SiO_2 catalytic performance in hydrodeoxygenation of anisole as model bio-oil compound: Suppression of benzene ring hydrogenation and C–C bond hydrogenolysis. *Chin. J. Catal.* **2017**, *38*, 1818–1830. [CrossRef]

43. Saguì, N.A.; Ström, P.; Edvinsson, T.; Pehlivan, I.B. Nickel Site Modification by High-Valence Doping: Effect of Tantalum Impurities on the Alkaline Water Electro-Oxidation by NiO Probed by Operando Raman Spectroscopy. *ACS Catal.* **2022**, *12*, 6506–6516. [CrossRef] [PubMed]

44. Fu, Y.; Pichon, B.; Devred, F.; Singleton, M.L.; Hermans, S. Synthesis of spherical, rod, or chain Ni nanoparticles and their structure–activity relationship in glucose hydrogenation reaction. *J. Catal.* **2022**, *415*, 63–76. [CrossRef]

45. Xu, J.; Zhu, P.; El Azab, I.H.; Bin Xu, B.; Guo, Z.; Elnaggar, A.Y.; Mersal, G.A.; Liu, X.; Zhi, Y.; Lin, Z.; et al. An efficient bifunctional Ni-Nb_2O_5 nanocatalysts for the hydrodeoxygenation of anisole. *Chin. J. Chem. Eng.* **2022**, *49*, 187–197. [CrossRef]

46. Yang, F.; Liu, D.; Zhao, Y.; Wang, H.; Han, J.; Ge, Q.; Zhu, X. Size Dependence of Vapor Phase Hydrodeoxygenation of *m*-Cresol on Ni/SiO_2 Catalysts. *ACS Catal.* **2018**, *8*, 1672–1682. [CrossRef]

47. Peck, M.A.; Langell, M.A. Comparison of Nanoscaled and Bulk NiO Structural and Environmental Characteristics by XRD, XAFS, and XPS. *Chem. Mater.* **2012**, *24*, 4483–4490. [CrossRef]

48. Wagner, C.D.; Gale, L.H.; Raymond, R.H. Two-dimensional chemical state plots: A standardized data set for use in identifying chemical states by X-ray photoelectron spectroscopy. *Anal. Chem.* **1979**, *51*, 466–482. [CrossRef]

49. Gaskell, K.J.; Starace, A.; Langell, M.A. ZnxNi1-xO Rocksalt Oxide Surfaces: Novel Environment for Zn2+ and Its Effect on the NiO Band Structure. *J. Phys. Chem. C* **2007**, *111*, 13912–13921. [CrossRef]

50. Shabaker, J.; Simonetti, D.; Cortright, R.; Dumesic, J. Sn-modified Ni catalysts for aqueous-phase reforming: Characterization and deactivation studies. *J. Catal.* **2005**, *231*, 67–76. [CrossRef]

51. Hu, X.; Yang, J.; Sun, W.; Wang, N.; An, S.; Wang, Q.; Zhang, Y.; Xie, X.; Huang, L. Y-Zr-O solid solution supported Ni-based catalysts for hydrogen production via auto-thermal reforming of acetic acid. *Appl. Catal. B Environ.* **2020**, *278*, 119264. [CrossRef]

52. Mateo, D.; Albero, J.; García, H. Graphene supported NiO/Ni nanoparticles as efficient photocatalyst for gas phase CO_2 reduction with hydrogen. *Appl. Catal. B Environ.* **2018**, *224*, 563–571. [CrossRef]

53. Zhang, M.; Zhang, J.; Zhou, Z.; Chen, S.; Zhang, T.; Song, F.; Zhang, Q.; Tsubaki, N.; Tan, Y.; Han, Y. Effects of the surface adsorbed oxygen species tuned by rare-earth metal doping on dry reforming of methane over Ni/ZrO_2 catalyst. *Appl. Catal. B Environ.* **2020**, *264*, 118522. [CrossRef]

54. Petitto, S.C.; Marsh, E.M.; Langell, M.A. Adsorption of Bromobenzene on Periodically Stepped and Nonstepped NiO(100). *J. Phys. Chem. B* **2005**, *110*, 1309–1318. [CrossRef]

55. Song, T.; Li, R.; Wang, J.; Dong, C.; Feng, X.; Li, S.; Mu, R.; Fu, Q. Selective oxidation of methane to CO on Ni@BOx via reaction-induced vapor migration of boron-containing species onto Ni. *Appl. Catal. B Environ.* **2023**, *321*, 122021. [CrossRef]

56. Zhao, D.; Shu, S.; Zhao, J.; Liang, Y.; Wang, H.; Liu, H.; Li, L.; Wang, D. Interactions of H_2O and O_2 with char during gasification in mixed atmosphere analyzed by isotope tracer method and in-situ DRIFTS. *Fuel* **2023**, *337*, 127173. [CrossRef]